



RESEARCH ARTICLE

Flame-assisted ultrafast synthesis of functionalized carbon nanosheets for high-performance sodium storage

Chen Chen^{1,2,3}  | Dong Yan⁴ | Yew Von Lim² | Lei Liu⁵ | Xue Liang Li² | Junjie Chen¹ | Tian Chen Li² | Youyu Zhu⁵ | Jiangtao Cai⁵ | Ying Huang¹ | Yating Zhang⁵ | Hui Ying Yang² 

¹School of Chemistry and Chemical Engineering, Northwestern Polytechnical University, Xi'an, China

²Pillar of Engineering Product Development, Singapore University of Technology and Design, Singapore, Singapore

³School of Electrical Engineering, Xi'an University of Technology, Xi'an, China

⁴International Joint Laboratory of New Energy Materials and Devices of Henan Province, School of Physics and Electronics, Henan University, Kaifeng, China

⁵College of Chemistry and Chemical Engineering, Xi'an University of Science and Technology, Xi'an, China

Correspondence

Ying Huang, School of Chemistry and Chemical Engineering, Northwestern Polytechnical University, 710072 Xi'an, China.

Email: yingh@nwpu.edu.cn

Yating Zhang, College of Chemistry and Chemical Engineering, Xi'an University of Science and Technology, 710054 Xi'an, China.

Email: isyating@163.com

Hui Ying Yang, Pillar of Engineering Product Development, Singapore University of Technology and Design, 8 Somapah Rd, Singapore 487372, Singapore.

Email: yanghuiying@sutd.edu.sg

Funding information

National Natural Science Foundation of China, Grant/Award Numbers: 51872236, 52072307; MOE SUTD Kickstarter Initiative, Grant/Award Number: SKI2021_02_16

Abstract

The unique structural features of hard carbon (HC) make it a promising anode candidate for sodium-ion batteries (SIB). However, traditional methods of preparing HC require special equipment, long reaction times, and large energy consumption, resulting in low throughputs and efficiency. In our contribution, a novel synthesis method is proposed, involving the formation of HC nanosheets (NS-CN) within minutes by creating an anoxic environment through flame combustion and further introducing sulfur and nitrogen sources to achieve heteroatom doping. The effect of heterogeneous element doping on the microstructure of HC is quantitatively analyzed by high-resolution transmission electron microscopy and image processing technology. Combined with density functional theory calculation, it is verified that the functionalized HC exhibits stronger Na⁺ adsorption ability, electron gain ability, and Na⁺ migration ability. As a result, NS-CN as SIB anodes provide an ultrahigh reversible capacity of 542.7 mAh g⁻¹ at 0.1 A g⁻¹, and excellent rate performance with a reversible capacity of 236.4 mAh g⁻¹ at 2 A g⁻¹ after 1200 cycles. Furthermore, full cell assembled with NS-CN as the can present 230 mAh g⁻¹ at 0.5 A g⁻¹ after 150 cycles. Finally, in/ex situ techniques confirm that the excellent sodium storage properties of NS-CN are due to the construction of abundant active sites based on the novel synthesis method for realizing the reversible adsorption of Na⁺. This work provides a novel strategy to develop novel carbons and gives deep insights for the further investigation of facile preparation methods to develop high-performance carbon anodes for alkali-ion batteries.

This is an open access article under the terms of the Creative Commons Attribution License, which permits use, distribution and reproduction in any medium, provided the original work is properly cited.

© 2024 The Authors. *Carbon Energy* published by Wenzhou University and John Wiley & Sons Australia, Ltd.

KEYWORDS

carbon nanosheets, heteroatom doping, sodium-ion battery, sustainable materials

1 | INTRODUCTION

After decades of development, lithium-ion battery (LIB) is one of the most successful secondary batteries with high energy density and safety.¹ Nonetheless, the global distribution of lithium resources, coupled with various constraints, has contributed to an escalation in its cost and has presented challenges in its application for large-scale grid-level energy storage systems. Recently, sodium-ion battery (SIB) has been considered an ideal supplement for LIB due to its similar physicochemical and electrochemical attributes and ubiquitous sodium resources.^{2–4} Meanwhile, the production line of LIB can serve as a similar production of SIB to further save production costs, whereas graphite, the commercial anode for LIB, fails to provide excellent Na^+ storage performances due to the unstable thermodynamic properties and inadequate ionic activation.⁵ Hard carbon (HC), composed of abundant pores, defects, and graphitic crystallites, has been demonstrated as a potential SIB anode material, providing highly reversible capacity and suitable working potential by integrating Na^+ storage mechanisms of adsorption, insertion, and pore-filling.^{6–8}

However, traditional HC materials face challenges of poor rate and cycling capabilities. A prevalent approach involves structural modification of HC materials through heteroatom doping (e.g., N, S, P, and B). This method leads to the creation of a profusion of active sites, thereby augmenting electrochemical kinetics.^{9,10} Another strategy is constructing unique carbon morphologies (such as microspheres, nanotubes, nanosheets, and fibers) to provide a stable host structure for ion/electron storage and a shortened distance for ion/electron diffusion.^{11–13} To synthesize the high-quality modified carbons, scientists usually employed some special equipment such as an electrospinning machine,^{14,15} microwave heater,^{16,17} spark plasma sintering,¹⁸ or a combination of these devices, which were usually expensive and exhibit high energy consumption. Besides, the corresponding synthesis process may face some challenges, including low throughput and complex preprocessing steps.^{19,20} In addition, some reported HCs were directly prepared from nonrenewable fossil resources or expensive precursors, which were against the basic foundation of sustainability. Therefore, it is urgent to reduce energy consumption, save cost, simplify the synthesis process, and rationally design HCs with excellent electrochemical performance.

Herein, we proposed a facile and fast ethanol flame combustion strategy to develop a kind of N-, S-, and O-

codoped carbon nanosheet. Sucrose was used as a carbon source. During the combustion process, CO_2 , NH_3 , SO_2 , and other gases are generated by the decomposition of NaHCO_3 . Thiourea was used to isolate air, inhibit the combustion of carbon sources, and push the carbon materials away from the flame area. Meanwhile, varieties of N- and S-containing by-products were generated by pyrolysis of thiourea, and the precursor could be doped by N and S elements in an oxygen-deficient environment with the assistance of an ethanol flame. The synthesis of heteroatom-doped carbon nanosheets could be completed in minutes. Further experimental results and density functional theory (DFT) calculations demonstrated that this novel strategy could not only endow carbons with abundant active sites to promote Na^+ adsorption but also provide ideal transport channels for Na^+ diffusion. As a result, the functionalized carbon nanosheets as SIB anodes exhibited excellent sodium storage performance, with a high specific capacity (542.7 mAh g^{-1} at 100 mA g^{-1}), superior rate performance (97.2 mAh g^{-1} at 10 A g^{-1}), and excellent cycling capability (capacity retention 236.4 mAh g^{-1} after 1200 cycles at 2 A g^{-1}). Furthermore, a full cell based on the as-prepared HC anodes delivered excellent electrochemical performances. This study presented a novel approach to designing functionalized carbon nanosheets for excellent Na^+ storage performances.

2 | RESULTS AND DISCUSSION

Figure 1A illustrates the growth of the functionalized carbon nanosheets (NS-CN). Ethanol was used as fuel, sucrose and thiourea served as carbon, nitrogen, and sulfur sources, and sodium bicarbonate was employed as a structural control agent. Here, the carbon samples without thiourea addition are labeled as CN, and the samples with different thiourea addition ratios are labeled as NS-CN-1, NS-CN-2, and NS-CN-3, respectively. Thermogravimetric-Fourier transform infrared (TG-FTIR, Figures 1B and S1) is applied to analyze the changes of various components during flame combustion. During the whole reaction process, NaHCO_3 in the mixture was thermally decomposed to produce a large amount of CO_2 gas ($2\text{NaHCO}_3 \rightarrow \text{Na}_2\text{CO}_3 + \text{CO}_2 + \text{H}_2\text{O}$).²¹ The huge number of CO_2 can not only promote the expansion and growth of the reactants but also dilute the air around the sample, reduce the O_2 concentration, and play a role in gas-phase flame

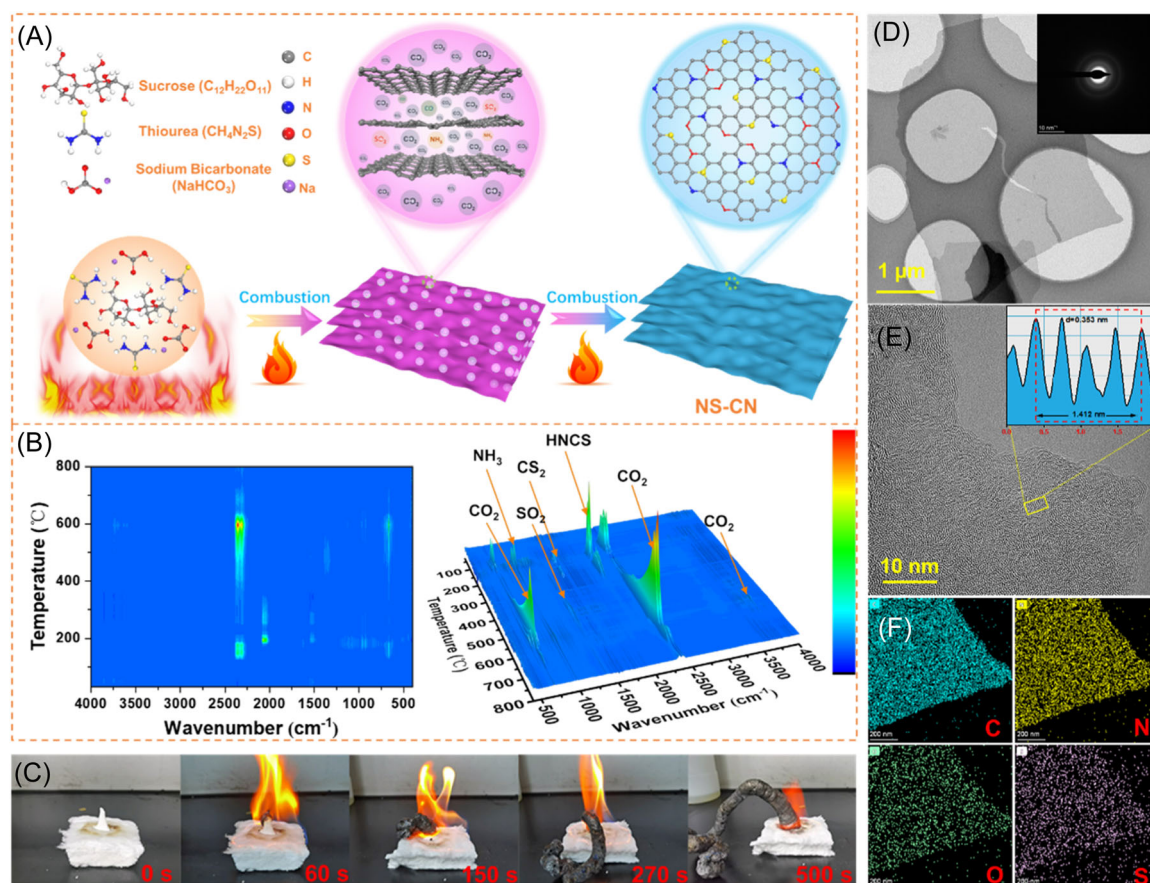


FIGURE 1 (A) Schematic illustration of NS-CN-2. (B) Two-dimensional (2D) and 3D TG-FTIR of NS-CN-2 precursors. (C) Digital photos of NS-CN-2 at different times. (D) TEM image (the inset is corresponding SAED pattern). (E) HRTEM image (the inset is lattice distance). (F) EDS mappings of NS-CN-2.

retardancy to prevent the complete combustion of sucrose.²² Thiourea has low thermal stability, and the thermal decomposition will not only generate HNCS, NH_3 , CS_2 , and SO_2 gases but also produce by-products such as sulfur and urea.²³ While sucrose gradually dehydrated into carbon with the generation of some carbon oxidizes under the limited O_2 concentration, most of the carbon expanded and extended outward under the push of abundant gas. Finally, the thermal decomposition products of thiourea reacted with sucrose to form N, S-doped carbon materials under ethanol flame-assisted ($\sim 550^\circ\text{C}$) in a local anoxic environment (Figure 1C).^{22,24} As shown in the video footage (Supporting Information), the black columnar reactants continued to expand and grow until the white powder was completely consumed by the thermal motivation. The whole reaction process took less than 10 min.

Scanning electron microscopy (SEM) (Figure S2) and transmission electron microscopy (TEM) (Figures 1D and S3A) images indicate that both CN and NS-CN-2 exhibit an irregular sheet-like structure, attributed to the overflow

and formation of the microstructure motivated by the gases such as CO_2 formation during the rapid synthesis. The selected area electron diffraction (SAED) pattern shows no obvious diffraction ring of NS-CN-2, suggesting its amorphous feature. High-resolution TEM (HRTEM) images of CN (Figure S3B) and NS-CN-2 (Figure 1E) show the characteristics of HC with short-range ordered and long-range disordered carbon grains. Lattice spacing measurements on the ordered parts indicate interlayer spacing of 0.403 and 0.353 nm for CN and NS-CN-2, respectively, which is consistent with the X-ray diffraction results (Figure S4). It was reported that the decreased interlayer spacing after doping is mainly due to the fact that S heteroatoms tend to be doped at defect sites of HC.^{10,25,26} Energy-dispersive spectra (EDS) elemental mapping images (Figures S3C and 1F) indicate that C, O, N, and S are uniformly distributed within the sample. Atomic force microscopy (Figure S5) shows that the thickness of NS-CN-2 sheets is about 1.7 nm, which facilitates the fast transport of Na^+ .^{27–29} According to N_2 adsorption/desorption data (Figure S6), the specific surface area of NS-CN is much

larger than that of CN, which is attributed to the corrosive gas generated by the pyrolysis of thiourea and the nanopores caused by heteroatom doping. The large specific surface area ensures adequate contact between the electrolyte and active materials, providing enhanced ionic activation.^{30–32}

To determine the effect of heteroatom functionalization on the microstructure of the carbon material, Fourier transform and inverse fast Fourier transform were conducted on the HRTEM image (Figure S7A,B), and ArcGIS software was used to extract the stripe structure in the carbon skeleton to obtain a binarized image (Figure S7C,D).^{33–35} According to the length of the lattice fringe, it is divided into three parts ($L \geq 0.3$ nm, $0.09 \leq L < 0.3$ nm, and $L < 0.09$ nm) with different colors (black, blue, and red; Figure 2A,B). Compared to CN, there are more red lattice fringes and curved lattice fringes in NS-CN. The number of lattice fringes with a length less than 0.09 nm in NS-CN-2 increased from 52.35% to 69%, indicating that the size of graphite crystallites in NS-CN decreased (Figure 2C). The lattice fringe orientation distribution of NS-CN-2 (Figure 2E) is also more uniformly distributed than CN's (Figure 2D),

demonstrating that the carbon structure tends to be more disordered with functionalization. Meanwhile, Raman spectra (Figure 3A and Table S1) and electron paramagnetic resonance (EPR, Figure 3B) spectra also show that NS-CN-2 has less sp^2 planar carbons and more defects and heteroatom doping contents. The above results show that the effective introduction of N and S elements could suppress the graphitization of carbon materials and distort the carbon layer due to the exposed abundant active sites, promoting the efficient capture of Na^+ .

The chemical composition of the carbon material was further investigated by X-ray photoelectron spectroscopy (XPS). As shown in Figure 3C, NS-CN-2 consists of C, N, O, and S elements, which is consistent with the results of EDS. To quantitatively obtain the specific content of elements, the content of each element in NS-CN-2 and CN is determined using an organic element analyzer (Table S2). The total content of O, N, and S in NS-CN-2 can be as high as 41.12%, and the abundant defects and heteroatoms would contribute more active sites to promote Na^+ capture.^{36,37} XPS results of C 1s (Figure S8) indicate that N and S elements are

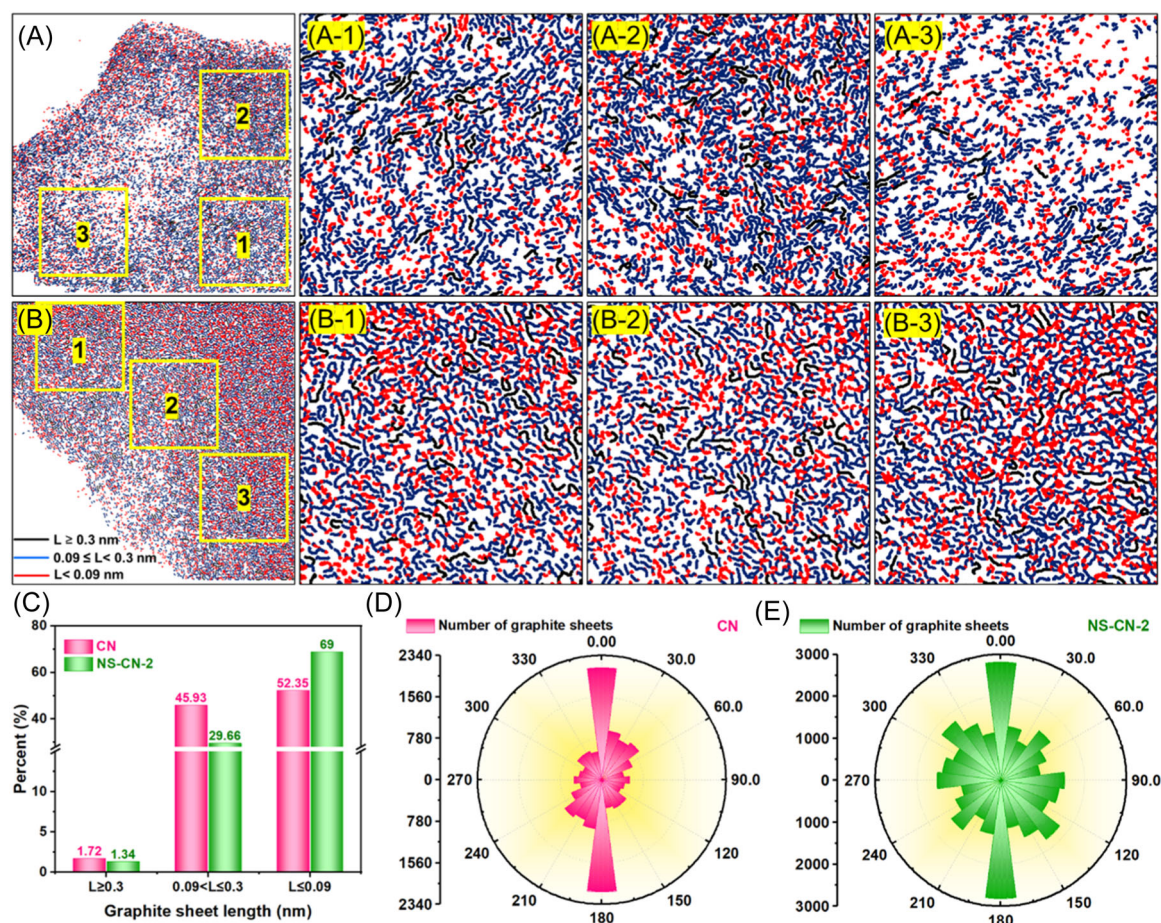


FIGURE 2 False-colored micrograph of (A) CN and (B) NS-CN-2 by length (the part marked with numbers is a partially enlarged view). (C) Length distribution of graphite fringe; graphite fringe orientation distribution of (D) CN and (E) NS-CN-2.

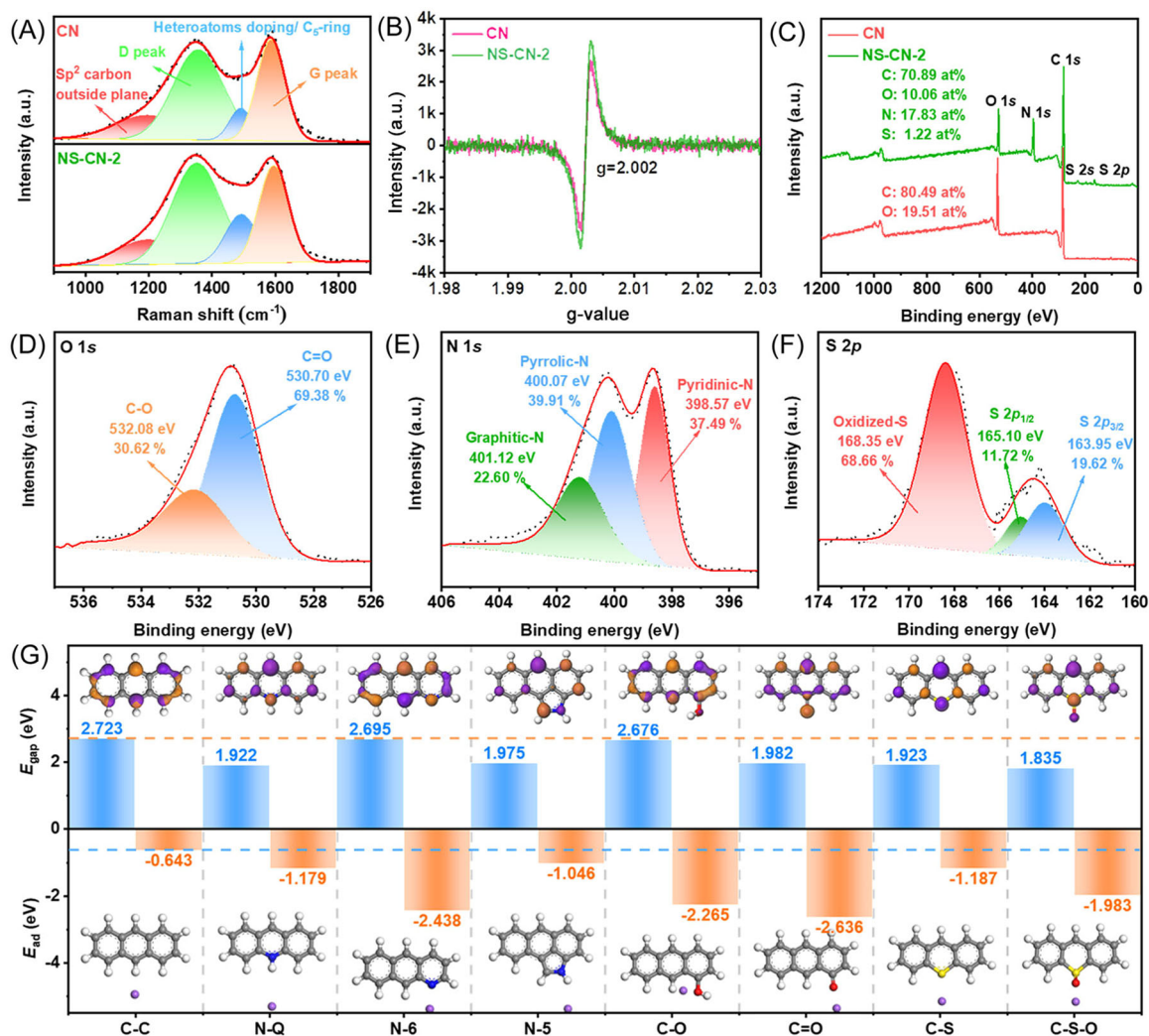


FIGURE 3 (A) Raman spectra, (B) EPR spectra, (C) XPS survey spectra, and high-resolution XPS spectra of (D) O 1s, (E) N 1s, and (F) S 2p of various samples. (G) Energy energy gaps and adsorption energies of different bonding types.

successfully doped into the carbon skeleton with carbon bonding. The high-resolution spectrum of O 1s (Figures 3D and S9) can be fitted with two peaks, corresponding to C–O (532.08 eV) and C=O (530.70 eV), respectively, and it was reported that a higher C=O bond content could help to improve the reversible capacity of carbons.^{38,39} N 1s spectrum (Figure 3E) can be fitted to three peaks of pyridinic-N (398.57 eV), pyrrolic-N (400.07 eV), and graphitic-N (401.12 eV). Pyridinic-N and pyrrolic-N usually exhibit high electrochemical activity, which can enhance the surface-induced capacitance and improve the Na⁺ diffusion capacity.^{40,41} In addition, the S element spectrum (Figure 3F) can be divided into three peaks, two of which are S 2p_{3/2} (163.95 eV) and S 2p_{1/2} (165.10 eV) representing C–S–C covalent bonds, and the other is oxidized-S (168.35 eV). S atoms are mainly located in defects and edges in the carbon structure, which would tend to distort the carbon structure and thus construct more Na⁺ storage sites.^{31,42,43}

It is well known that different bond types of heteroatoms show different adsorption capacities and reactivities for Na⁺.^{44–46} Therefore, the bonding type between heteroatoms and carbon was determined by peak fitting of O, N, and S spectra, in which the effect of heteroatoms on electrochemical performance is further evaluated by DFT calculations. Since the electronegativities of N (3.04) and O (3.44) atoms are higher than that of the carbon (2.55) atom, the introduction of N and O atoms can attract the surrounding electrons, thereby making themselves an electron-rich state, which is helpful for the adsorption of Na⁺ (Figure S10). Although the electronegativity of the sulfur (2.58) atom is close to that of carbon, when it combines with the oxygen atom to form a C–S–O bond, this unique combination can produce orbitals different from that of the neutral C and affect the Mulliken charge of surrounding atoms. By observing the energy gap (E_{gap}) of the molecular frontier

orbital (Figure 3G and Table S3), the smaller energy gap generally exhibits higher reactivity. Heteroatom doping can improve electronic conductivity and reactivity in stark contrast to the pure carbon (pure-C) model. Adsorption energy results (E_{ad} ; Table S4) confirm that heteroatom doping can significantly improve the capture ability of carbon materials for Na^+ , among which N-6, C=O, and C-S-O bonds have the strongest adsorption capacity for Na^+ . Besides, the above three chemical bonds are relatively high in NS-CN-2, implying that NS-CN-2 has a strong Na^+ adsorption capacity.

The electrochemical performance of the anode material was analyzed in a half-cell system. Figure S11 shows cyclic voltammetry (CV) curves of the CN and NS-CN-2 at 0.1 mV s^{-1} . Both samples show different profiles. In the first cycle, NS-CN-2 exhibits a large irreversible reduction peak. This is attributed to the large specific surface area and abundant heteroatom functional groups, resulting in the generation of solid-state electrolyte interfacial (SEI) films. In the subsequent cycles, NS-

CN-2 does not display an obvious redox peak around $0.2/0.01 \text{ V}$, different from the pristine CN sample, indicating that the sodium storage behavior of NS-CN-2 is an adsorption-dominated capacitive behavior.¹⁰ It is worth mentioning that there is no redox peak generated by the reaction of elemental S in the CV curve, indicating that S is mainly doped into the carbon structure, thereby generating active sites to capture Na^+ . Figures 4A and S12 show that the initial discharge/charge capacities of NS-CN and CN are $1189.7/490.3$ and $465.2/201.7 \text{ mAh g}^{-1}$, with initial Coulombic efficiencies of 41.2% and 43.3% at 0.1 A g^{-1} , respectively. From the second cycle to the tenth cycle, their galvanostatic charge–discharge (GCD) profiles are identical, indicating excellent electrochemical kinetic properties and performance stability. Figure 4B shows the cycling performance of carbons. NS-CN-2 exhibits a highly reversible capacity of 541.4 mAh g^{-1} at 0.2 A g^{-1} after 400 cycles, with an excellent capacity retention of around 100%. It is worth noting that the reversible capacity first increases and

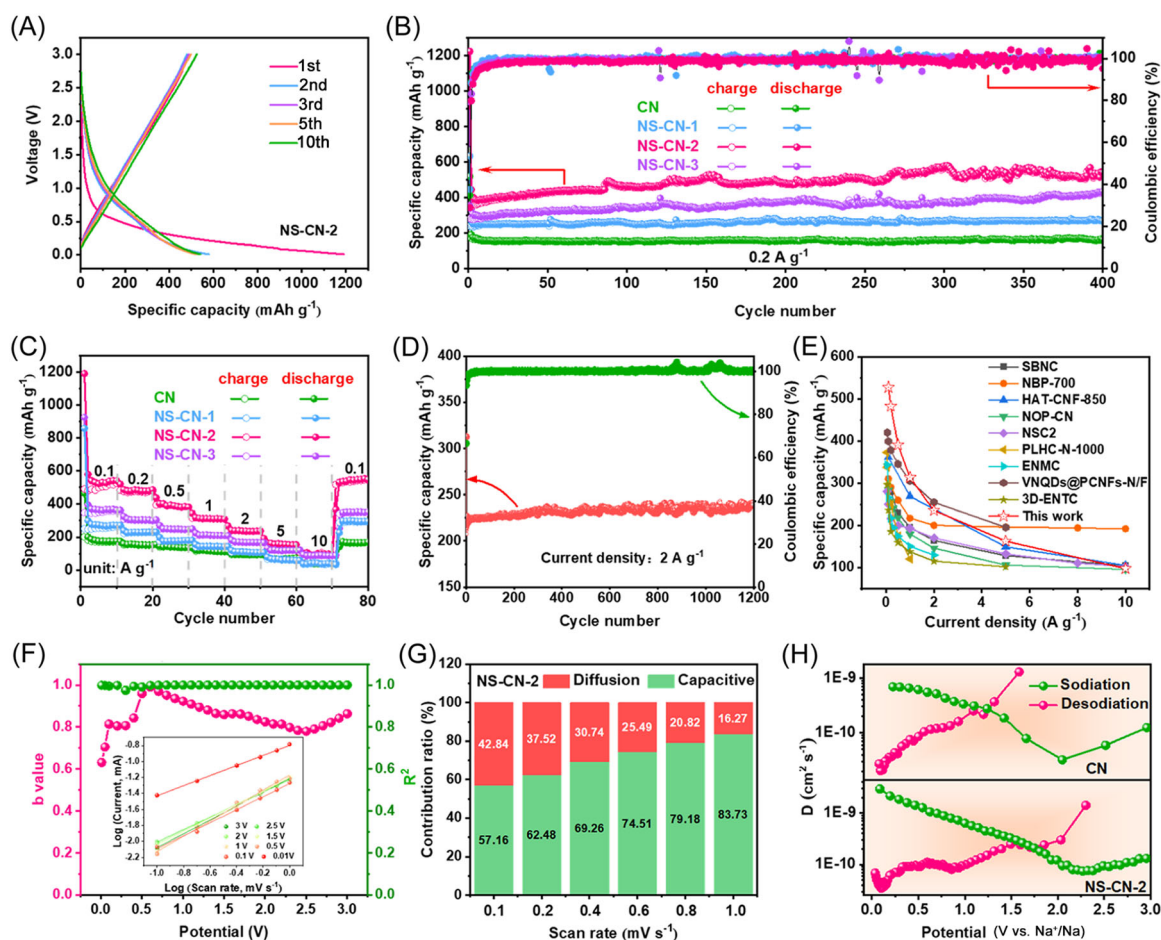


FIGURE 4 (A) GCD curve of NS-CN-2 at 0.1 A g^{-1} . (B) Cyclic performances. (C) Rate performances. (D) Long cycle performance of NS-CN-2. (E) Comparisons of rate performances. (F) b Value at different operation states. The inset is $\log(\text{scan rate})$ versus $\log(\text{peak current})$. (G) Capacitive contribution. (H) D_{Na^+} of CN and NS-CN-2 during sodiation/desodiation process.

then stabilizes at the subsequent cycles, which is attributed to the activation of porous materials.^{47–49} Figure 4C indicates reversible capacities of 540.1, 484.9, 390.1, 314.5, 237.2, 158.3, and 97.2 mAh g^{−1} for NS-CN-2 at 0.1, 0.2, 0.5, 1, 2, 5, and 10 A g^{−1}, respectively. When the current density is restored to 100 mA g^{−1}, the reversible capacity recovered to 542.7 mAh g^{−1}, indicating excellent rate capability. Figure S13 shows the GCD curves of NS-CN-2 at different current densities with lower polarization, indicating excellent electrochemical kinetics. Meanwhile, compared with CN at the same current density, the NS-CN-2 exhibits higher capacity in the high voltage region (1–3 V), indicating that the abundance of heteroatoms and pores could induce more electrochemical active sites. Subsequently, the long-term cycling stability of sodium storage capacity for NS-CN-2 (Figure 4D) was evaluated at 2 A g^{−1}, and the reversible capacity was maintained at 236.4 mAh g^{−1} after 1200 cycles, showing excellent cycling stability. As compared with other reported advanced carbon anodes (Figure 4E and Table S5), the NS-CN-2 presents more excellent electrochemical performances.^{10,28,50–56} Interfacial resistance (R_s) and charge transfer resistance (R_{ct}) of the carbon materials are evaluated through electrochemical impedance spectra (Figures S14 and S15). In comparison, the R_s and R_{ct} of NS-CN-2 are smaller, indicating the enhanced charge transfer ability of carbon materials after modification. As cycling progresses, the impedance of NS-CN-2 and CN (Figure S16) gradually decreases; this can be attributed to the gradual infiltration of electrolytes and the stabilization of carbon structure during repeated sodiation/desodiation.⁵⁷

Generally, the sodium storage process of HC is mainly divided into a diffusion-controlled intercalation process and a surface-induced capacitance process. Figure 4F shows the evaluation of different-state b value (b values of 0.5 and 1.0 indicate diffusion-controlled and surface capacitive-controlled processes, respectively; please see detailed calculation in Supporting information). Except for the b Value of 0.6 near 0.01 V, the b Value of the other voltages is above 0.7, indicating that NS-CN-2 shows a hybrid sodium storage mechanism dominated by capacitive processes.^{58,59} In addition, the proportion of the capacitance contribution for CN and NS-CN-2 in the sodium storage process is further quantitatively analyzed, and the surface-induced capacitance contributions of CN and NS-CN-2 are 80.37% and 83.73% at 1 mV s^{−1}, respectively (Figure S17). Meanwhile, the capacitance contribution of NS-CN-2 is higher than that of CN at different scan rates (Figures 4G and S18). This is mainly due to the abundant surface functional groups and high specific surface area of modified carbons for improving electrochemical kinetics. The diffusion behavior of Na⁺ in carbon materials can be observed by the galvanostatic intermittent

titration technique curve (Figure S19). The trends of Na⁺ diffusion in CN and NS-CN-2 are similar during the sodiation/desodiation process (Figure 4H). In comparison, the NS-CN-2 shows a higher Na⁺ diffusion coefficient (D_{Na^+}), indicating the boosted Na⁺ diffusion kinetics after N and S doping.

Changes in microstructure and chemical composition of electrode materials are observed via ex situ studies. Ex situ TEM images of NS-CN-2 after 400 cycles (Figure S20) indicate that the nanosheets maintained their initial microstructural morphology, demonstrating excellent structure stability after long-term cycling. HRTEM images (Figure 5A,B) also reveal that the overall microstructure is maintained with indicated short- and long-ranged disorder even after long cycles. It is worth noting that the graphite interlayer spacing of carbon (Figure 5C) increased by only 9.9% after repeated sodiation/desodiation processes, further confirming the stable microstructure. In situ Raman tests (Figure 5D) show that the intensity ratio of the defect or disorder-induced D band and the first-order graphite G band (I_D/I_G) decreases during the discharging process and increases during the charging process. This indicates that Na⁺ is adsorbed at graphitic defect sites during the sodiation process with high reversibility. Ex situ XPS (Figure 5E) spectra show that peak intensities of C=O bond and pyrrolic-N first decrease at the sodiation process and then return to the original intensities after the next desodiation processes, further indicating the high structure reversibility.^{38,60} Notably, peak intensities of S 2p and graphitic-N could not fully recover to the initial intensities during cycling, demonstrating partial reversibility of functional groups.^{61,62} Moreover, oxidized-S bond and pyridinic-N peaks show high reversibility during cycling, further supporting the dominant Na⁺ adsorption reaction mechanism.

The effects of N and S doping on Na⁺ adsorption, diffusion barrier, and electronic conductivity were further evaluated by DFT calculations. Since carbon materials usually contain defects and oxygen elements, four models of pure-C, defective carbon (defect-C), oxygen-doped carbon (O-C), and N/O/S-doped carbon (N/O/S-C) were established for the situation. Figure 5F shows that the Na⁺ adsorption kinetics of pure-C is unstable, and the introduction of defects can slightly improve the Na⁺ adsorption kinetics. The adsorption energy of NOS-C is much higher than those of the other three models. By comparing the differential charge densities of the four models, NOS-C has more charge accumulation, indicating that the introduction of N, S, and O can significantly enhance the capture ability of carbon materials for Na⁺. The diffusivity is assessed by evaluating the Na⁺ diffusion barrier (Figure S21). As compared with graphite, NOS-C has a lower Na⁺ diffusion barrier (Figure 5G), demonstrating better diffusivity. The density of states (DOS) (Figures S22 and 5H) shows that N, S, and O

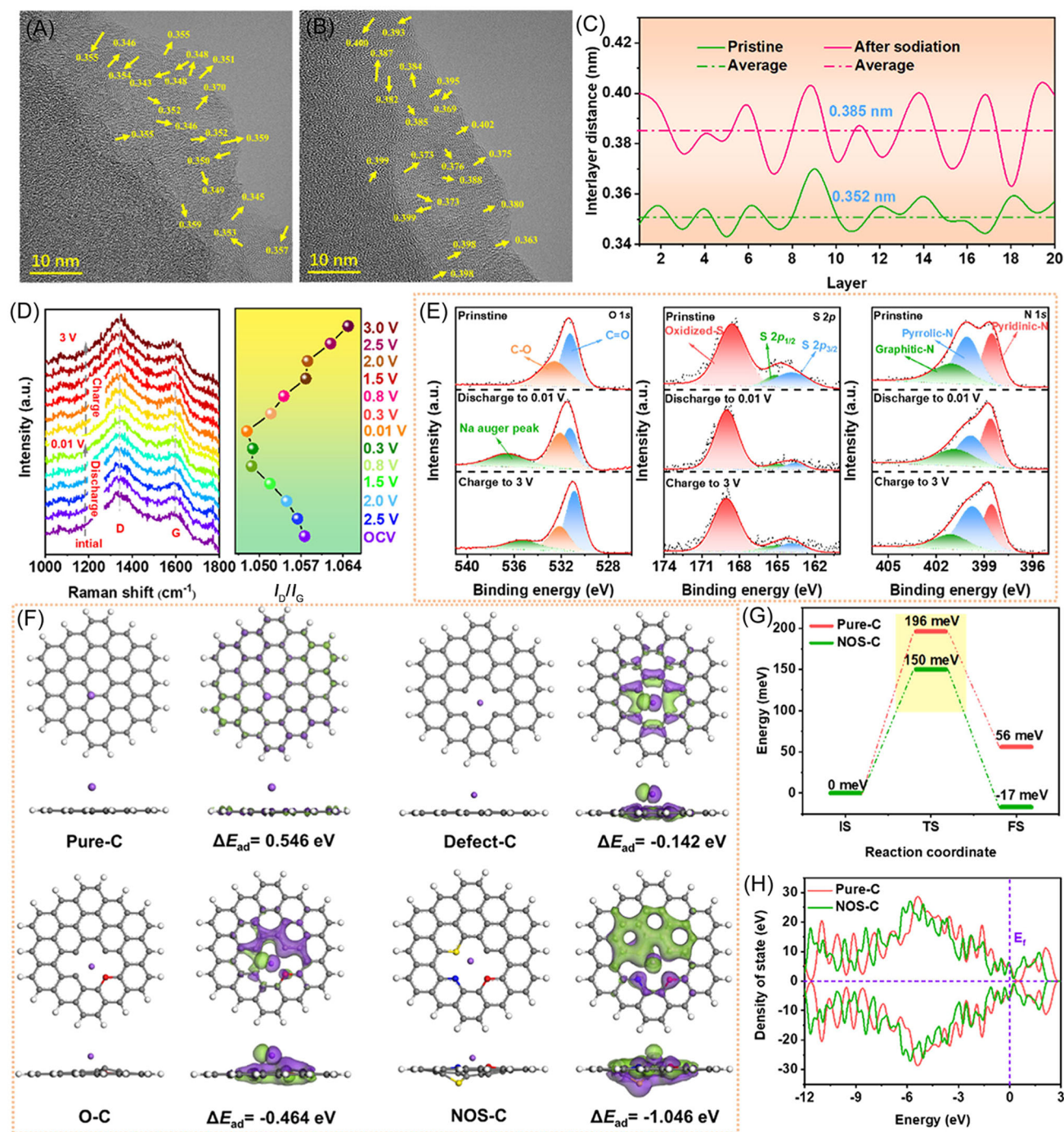


FIGURE 5 (A) The HRTEM image of pristine NS-CN-2. (B) The HRTEM image of NS-CN-2 after 400 cycles at 0.2 A g^{-1} . (C) Graph of graphite layer spacing change for CN and NS-CN-2. (D) In situ Raman of NS-CN-2. (E) Ex situ XPS of NS-CN-2. (F) Adsorption energy models and differential charge densities for pure-C, defect-C, O-C, and NOS-C. (G) Diffusion barrier of Na^+ in pure-C and NOS-C. (H) Density of states of pure-C and NOS-C.

doping can endow carbon with higher DOS at the Fermi level, indicating enhanced electronic conductivity.

To highlight the practical application prospect of NS-CN-2, we assembled coin-type full cells with NS-CN-2 as the anode material and $\text{Na}_3\text{V}_2(\text{PO}_4)_3$ (NVP) as the cathode material (Figure 6A). The NVP cathodes exhibit

stable cycling performance with a reversible capacity of 104.3 mAh g^{-1} at 0.1 A g^{-1} (Figure S23). According to the specific capacity of NS-CN-2 and NVP at 0.1 A g^{-1} (Figure 6B), the active mass ratio of the cathode to anode in the full cell is about 5:1. Before assembling the full cell, NS-CN-2 is first cycled at 0.05 A g^{-1} for 10 cycles

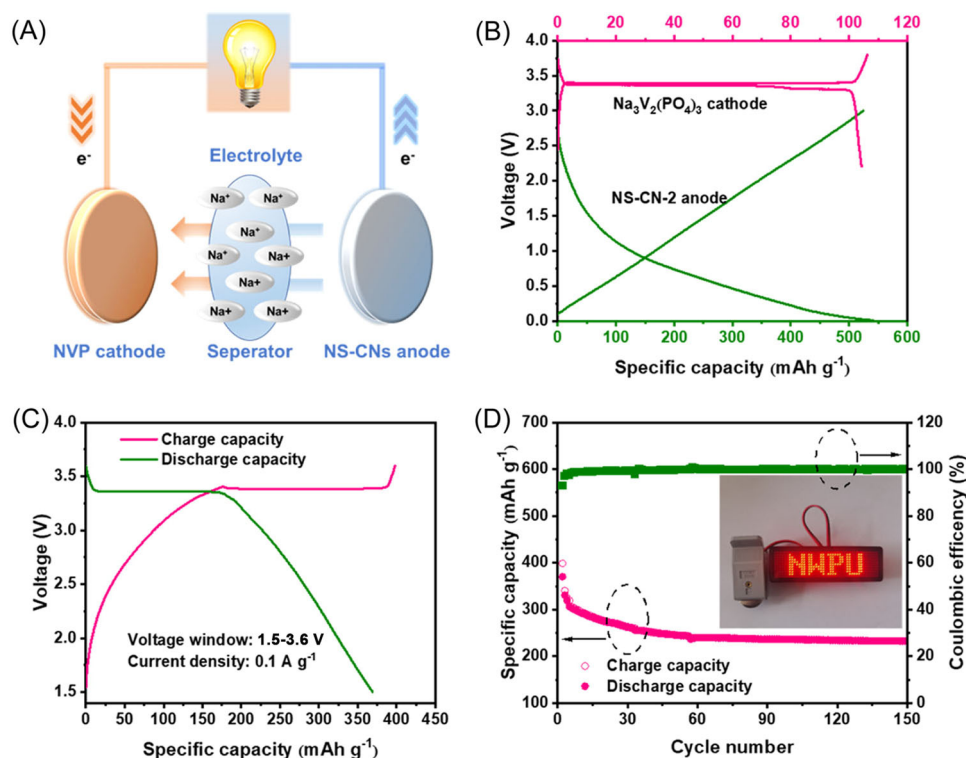


FIGURE 6 (A) Schematic diagram of an SIBs full cell. (B) GCD of the NVP and NS-CN-2 half cell at 0.1 A g⁻¹. (C) GCD of the NVP//NS-CN-2 full cell. (D) The cycling performance of NVP//NS-CN-2 full cell at 0.5 A g⁻¹ (the inset is the LED device showing “NWPU” by two full cells).

to form a stable SEI film. As shown in Figure 6C, the ICE of NVP//NS-CN-2 can reach 92% with the voltage window of 1.5–3.6 V. Meanwhile, NVP//NS-CN-2 can display a highly reversible capacity of 230 mAh g⁻¹ after 150 cycles at 0.5 A g⁻¹ (Figure 6D). The illustration shows that the light-emitting diode (LED) device with “NWPU” can be lit by two fully charged batteries in series.

3 | CONCLUSIONS

In summary, a novel and facile flame-assisted ultrafast combustion strategy was conducted to develop the N, S, and O codoped carbon nanosheet for high-performance SIB anodes. Under the high-temperature flame, NaHCO₃ decomposes to generate a large amount of CO₂ to dilute the air, inhibiting the oxidation of the precursor and promoting the nanosheets expansion growth. Meanwhile, thiourea provides abundant nitrogen and sulfur sources for the precursor and endows carbon with rich heteroatom doping content (41.12%) and nanosheet morphology under the high-temperature activation of the flame. As a result, the modified carbons exhibit excellent sodium storage properties with a high specific capacity (542.7 mAh g⁻¹ at 100 mA g⁻¹), superior rate performance (97.2 mAh g⁻¹ at

10 A g⁻¹), and excellent cycling capability (capacity retention 236.4 mAh g⁻¹ after 1200 cycles at 2 A g⁻¹). Furthermore, theoretical calculations and in/ex situ investigations reveal the effect of functionalized structures on the sodium storage properties of HC materials and confirm that the excellent sodium storage properties are attributed to the reversible adsorption of Na⁺ by designed defect sites and heteroatom groups. This study provides an efficient and versatile synthetic method to fabricate HC materials for further commercial applications.

ACKNOWLEDGMENTS

This work was supported by the National Natural Science Foundation of China (Grant Nos. 51872236, 52072307) and MOE SUTD Kickstarter Initiative (SKI 2021_02_16). The authors thank the Analytical & Testing Center of Northwestern Polytechnical University for scanning electron microscopy, transmission electron microscopy, and Raman spectroscopy.

CONFLICT OF INTEREST STATEMENT

The authors declare that there are no conflicts of interests.

ORCID

Chen Chen <http://orcid.org/0000-0002-3485-1618>

Hui Ying Yang <http://orcid.org/0000-0002-2244-8231>

REFERENCES

- Chou S, Yu Y. Next generation batteries: aim for the Future. *Adv Energy Mater.* 2017;7(24):1703223.
- Usiskin R, Lu Y, Popovic J, et al. Fundamentals, status and promise of sodium-based batteries. *Nat Rev Mater.* 2021;6(11):1020-1035.
- Liu M, Wang Y, Wu F, et al. Advances in carbon materials for sodium and potassium storage. *Adv Funct Mater.* 2022;32(31):2203117.
- Man Y, Sun J, Zhao X, et al. An ultrastable sodium-ion battery anode enabled by carbon-coated porous $\text{NaTi}_2(\text{PO}_4)_3$ olive-like nanospheres. *J Colloid Interface Sci.* 2023;635:417-426.
- Nobuhara K, Nakayama H, Nose M, Nakanishi S, Iba H. First-principles study of alkali metal-graphite intercalation compounds. *J Power Sources.* 2013;243:585-587.
- Chen X, Tian J, Li P, et al. An overall understanding of sodium storage behaviors in hard carbons by an "adsorption-intercalation/filling" hybrid mechanism. *Adv Energy Mater.* 2022;12(24):2200886.
- Thompson M, Xia Q, Hu Z, Zhao X-S. A review on biomass-derived hard carbon materials for sodium-ion batteries. *Mater Adv.* 2021;2(18):5881-5905.
- Wang Q, Zhu X, Liu Y, Fang Y, Zhou X, Bao J. Rice husk-derived hard carbons as high-performance anode materials for sodium-ion batteries. *Carbon.* 2018;127:658-666.
- Li Y, Chen M, Liu B, et al. Heteroatom doping: an effective way to boost sodium ion storage. *Adv Energy Mater.* 2020;10(27):2000927.
- Jin Q, Wang K, Feng P, Zhang Z, Cheng S, Jiang K. Surface-dominated storage of heteroatoms-doping hard carbon for sodium-ion batteries. *Energy Storage Mater.* 2020;27:43-50.
- Vijaya Kumar Saroja AP, Muruganathan M, Muthusamy K, Mizuta H, Sundara R. Enhanced sodium ion storage in interlayer expanded multiwall carbon nanotubes. *Nano Lett.* 2018;18(9):5688-5696.
- Li Y, Yuan Y, Bai Y, et al. Insights into the Na^+ storage mechanism of phosphorus-functionalized hard carbon as ultrahigh capacity anodes. *Adv Energy Mater.* 2018;8(18):1702781.
- Yin X, Lu Z, Wang J, et al. Enabling fast Na^+ transfer kinetics in the whole-voltage-region of hard-carbon anodes for ultrahigh-rate sodium storage. *Adv Mater.* 2022;34(13):2109282.
- Jia H, Sun N, Dirican M, et al. Electrospun kraft lignin/cellulose acetate-derived nanocarbon network as an anode for high-performance sodium-ion batteries. *ACS Appl Mater Interfaces.* 2018;10(51):44368-44375.
- Guo X, Zhang X, Song H, Zhou J. Electrospun cross-linked carbon nanofiber films as free-standing and binder-free anodes with superior rate performance and long-term cycling stability for sodium ion storage. *J Mater Chem A.* 2017;5(40):21343-21352.
- Yu K, Wang X, Yang H, Bai Y, Wu C. Insight to defects regulation on sugarcane waste-derived hard carbon anode for sodium-ion batteries. *J Energy Chem.* 2021;55:499-508.
- Li Z, Chen Y, Jian Z, et al. Defective hard carbon anode for Na-ion batteries. *Chem Mater.* 2018;30(14):4536-4542.
- Zhen Y, Chen Y, Li F, Guo Z, Hong Z, Titirici MM. Ultrafast synthesis of hard carbon anodes for sodium-ion batteries. *Proc Natl A Sci USA.* 2021;118(42):e2111119118.
- Chen X, Fang Y, Lu H, et al. Microstructure-dependent charge/discharge behaviors of hollow carbon spheres and its implication for sodium storage mechanism on hard carbon anodes. *Small.* 2021;17(34):2102248.
- Guo R, Lv C, Xu W, et al. Effect of intrinsic defects of carbon materials on the sodium storage performance. *Adv Energy Mater.* 2020;10(9):1903652.
- Toan S, O'Dell W, Russell CK, et al. Thermodynamics of NaHCO_3 decomposition during Na_2CO_3 -based CO_2 capture. *J Environ Sci.* 2019;78:74-80.
- Chen B, Wu D, Wang T, Yuan F, Jia D. Rapid preparation of porous carbon by flame burning carbonization method for supercapacitor. *Chem Eng J.* 2023;462:142163.
- Wang S, Gao Q, Wang J. Thermodynamic analysis of decomposition of thiourea and thiourea oxides. *J Phys Chem B.* 2005;109(36):17281-17289.
- Du X, Liu H-Y, Mai Y-W. Ultrafast synthesis of multi-functional N-doped graphene foam in an ethanol flame. *ACS Nano.* 2016;10(1):453-462.
- Hong Z, Zhen Y, Ruan Y, et al. Rational design and general synthesis of S-doped hard carbon with tunable doping sites toward excellent Na-ion storage performance. *Adv Mater.* 2018;30(29):1802035.
- Zhang Y, Li L, Xiang Y, et al. High sulfur-doped hard carbon with advanced potassium storage capacity via a molten salt method. *ACS Appl Mater Interfaces.* 2020;12(27):30431-30437.
- Xia J-L, Yan D, Guo L-P, et al. Hard carbon nanosheets with uniform ultramicropores and accessible functional groups showing high realistic capacity and superior rate performance for sodium-ion storage. *Adv Mater.* 2020;32(21):2000447.
- Jin Q, Li W, Wang K, et al. Tailoring 2D heteroatom-doped carbon nanosheets with dominated pseudocapacitive behaviors enabling fast and high-performance sodium storage. *Adv Funct Mater.* 2020;30(14):1909907.
- Xu G, Wang Q, Su Y, et al. Revealing electrochemical sodiation mechanism of orthogonal- Nb_2O_5 nanosheets by in situ transmission electron microscopy. *Acta Phys Chim Sin.* 2020;38(8):2009073.
- Wei Z, Ding B, Dou H, et al. 2020 roadmap on pore materials for energy and environmental applications. *Chin Chem Lett.* 2019;30(12):2110-2122.
- Liu Y, Qiao Y, Wei G, et al. Sodium storage mechanism of N, S co-doped nanoporous carbon: experimental design and theoretical evaluation. *Energy Storage Mater.* 2018;11:274-281.
- Zheng Y, Lu Y, Qi X, et al. Superior electrochemical performance of sodium-ion full-cell using poplar wood derived hard carbon anode. *Energy Storage Mater.* 2019;18:269-279.
- Liu L, Du M, Li G, et al. Structure and evolution features of cutinite with different coal rank from stacking and arrangement of aromatic fringes in HRTEM. *Fuel.* 2022;326:124998.
- Sharma A, Kyotani T, Tomita A. Quantitative evaluation of structural transformations in raw coals on heat-treatment using HRTEM technique. *Fuel.* 2001;80(10):1467-1473.
- Wang X, Wang S, Hao C, Zhao Y, Song X. Quantifying orientation and curvature in HRTEM lattice fringe micrographs of naturally thermally altered coals: new insights from a structural evolution perspective. *Fuel.* 2022;309:122180.
- Chen C, Huang Y, Lu M, Zhang J, Li T. Tuning morphology, defects and functional group types in hard carbon via

- phosphorus doped for rapid sodium storage. *Carbon*. 2021;183:415-427.
37. Qiao Y, Han R, Pang Y, et al. 3D well-ordered porous phosphorus doped carbon as an anode for sodium storage: structure design, experimental and computational insights. *J Mater Chem A*. 2019;7(18):11400-11407.
 38. Chen C, Huang Y, Zhu Y, et al. Nonignorable influence of oxygen in hard carbon for sodium ion storage. *ACS Sustainable Chem Eng*. 2020;8(3):1497-1506.
 39. Xu Z, Du S, Yi Z, et al. Water chestnut-derived slope-dominated carbon as a high-performance anode for high-safety potassium-ion batteries. *ACS Appl Energy Mater*. 2020;3(11):11410-11417.
 40. Shao W, Hu F, Song C, et al. Hierarchical N/S co-doped carbon anodes fabricated through a facile ionothermal polymerization for high-performance sodium ion batteries. *J Mater Chem A*. 2019;7(11):6363-6373.
 41. Huang M, Xi B, Feng Z, et al. Facile synthesis of N,O-codoped hard carbon on the kilogram scale for fast capacitive sodium storage. *J Mater Chem A*. 2018;6(34):16465-16474.
 42. Qie L, Chen W, Xiong X, et al. Sulfur-doped carbon with enlarged interlayer distance as a high-performance anode material for sodium-ion batteries. *Adv Sci*. 2015;2(12):1500195.
 43. Zhao G, Yu D, Zhang H, et al. Sulphur-doped carbon nanosheets derived from biomass as high-performance anode materials for sodium-ion batteries. *Nano Energy*. 2020;67:104219.
 44. He H, Huang D, Tang Y, et al. Tuning nitrogen species in three-dimensional porous carbon via phosphorus doping for ultra-fast potassium storage. *Nano Energy*. 2019;57:728-736.
 45. Huang H, Xu R, Feng Y, et al. Sodium/potassium-ion batteries: boosting the rate capability and cycle life by combining morphology, defect and structure engineering. *Adv Mater*. 2020;32(8):1904320.
 46. Yan D, Yang HY, Bai Y. Tactics to optimize conversion-type metal fluoride/sulfide/oxide cathodes toward advanced lithium metal batteries. *Nano Res*. 2023;16(6):8173-8190.
 47. Hou H, Shao L, Zhang Y, et al. Large-area carbon nanosheets doped with phosphorus: a high-performance anode material for sodium-ion batteries. *Adv Sci*. 2017;4(1):1600243.
 48. Senthil C, Park JW, Shaji N, Sim GS, Lee CW. Biomass seaweed-derived nitrogen self-doped porous carbon anodes for sodium-ion batteries: insights into the structure and electrochemical activity. *J Energy Chem*. 2022;64:286-295.
 49. Liu J, Zhang Y, Zhang L, et al. Graphitic carbon nitride (g-C₃N₄)-derived N-rich graphene with tuneable interlayer distance as a high-rate anode for sodium-ion batteries. *Adv Mater*. 2019;31(24):1901261.
 50. Tang Y, Wang X, Chen J, Wang D, Mao Z. Synthesis of presodiated B, N co-doped carbon materials and application in sodium ions batteries with enhanced initial Coulombic efficiency. *Chem Eng J*. 2022;427:131951.
 51. Yan R, Josef E, Huang H, et al. Understanding the charge storage mechanism to achieve high capacity and fast ion storage in sodium-ion capacitor anodes by using electrospun nitrogen-doped carbon fibers. *Adv Funct Mater*. 2019;29(26):1902858.
 52. Chen C, Huang Y, Meng Z, et al. N/O/P-rich three-dimensional carbon network for fast sodium storage. *Carbon*. 2020;170:225-235.
 53. Nie W, Cheng H, Liu X, et al. Surface organic nitrogen-doping disordered biomass carbon materials with superior cycle stability in the sodium-ion batteries. *J Power Sources*. 2022;522:230994.
 54. Huang S, Yang D, Qiu X, et al. Boosting surface-dominated sodium storage of carbon anode enabled by coupling graphene nanodomains, nitrogen-doping, and nanoarchitecture engineering. *Adv Funct Mater*. 2022;32(33):2203279.
 55. Yuan J, Qiu M, Hu X, et al. Pseudocapacitive vanadium nitride quantum dots modified one-dimensional carbon cages enable highly kinetics-compatible sodium ion capacitors. *ACS Nano*. 2022;16(9):14807-14818.
 56. Zhang W, Sun M, Yin J, et al. Rational design of carbon anodes by catalytic pyrolysis of graphitic carbon nitride for efficient storage of Na and K mobile ions. *Nano Energy*. 2021;87:106184.
 57. Yan D, Li K, Yan Y, et al. Cubic spinel XIn₂S₄(X = Fe, Co, Mn): a new type of anode material for superfast and ultrastable Na-ion storage. *Adv Energy Mater*. 2021;11(44):2102137.
 58. Yao X, Ke Y, Ren W, et al. Defect-rich soft carbon porous nanosheets for fast and high-capacity sodium-ion storage. *Adv Energy Mater*. 2018;9(6):1803260.
 59. Chen J, Wang T, Zhang F, Tian N, Zhang Q, Zhang B. The multicomponent synergistic effect of sandwich structure hierarchical nanofibers for enhanced sodium storage. *Small*. 2022;18(14):2107370.
 60. Zhao H, Ye J, Song W, et al. Insights into the surface oxygen functional group-driven fast and stable sodium adsorption on carbon. *ACS Appl Mater Interfaces*. 2020;12(6):6991-7000.
 61. Liu S, Zhou J, Song H. Tailoring highly N-doped carbon materials from hexamine-based MOFs: superior performance and new insight into the roles of N configurations in Na-ion storage. *Small*. 2018;14(12):1703548-1703556.
 62. Song W, Kan J, Wang H, et al. Nitrogen and sulfur Co-doped mesoporous carbon for sodium ion batteries. *ACS Appl Nano Mater*. 2019;2(9):5643-5654.

SUPPORTING INFORMATION

Additional supporting information can be found online in the Supporting Information section at the end of this article.

How to cite this article: Chen C, Yan D, Von Lim Y, et al. Flame-assisted ultrafast synthesis of functionalized carbon nanosheets for high-performance sodium storage. *Carbon Energy*. 2024;6:e482. doi:10.1002/cey2.482